PAPER

Neutron-rich rare isotope production with stable and radioactive beams in the mass range $A \sim$ 40–60 at beam energy around 15 MeV/nucleon

To cite this article: A Papageorgiou *et al* 2018 *J. Phys. G: Nucl. Part. Phys.* **45** 095105

View the article online for updates and enhancements.

Related content

Neutron-rich rare isotope production with stable and radioactive beams in the mass range $A \sim 40$–60 at beam energy around 15 MeV/nucleon

A Papageorgiou[1], G A Souliotis[1] , K Tshoo[2], S C Jeong[2], B H Kang[2], Y K Kwon[2], M Veselsky[3], S J Yennello[4] and A Bonasera[4,5]

[1] Laboratory of Physical Chemistry, Department of Chemistry, National and Kapodistrian University of Athens, Athens 15771, Greece
[2] The Rare Isotope Science Project (RISP), Institute for Basic Science, Daejeon, Republic of Korea
[3] Institute of Physics, Slovak Academy of Sciences, Bratislava 84511, Slovakia
[4] Cyclotron Institute, Texas A&M University, College Station, TX, United States of America
[5] Laboratori Nazionali del Sud, INFN, Catania, Italy

E-mail: soulioti@chem.uoa.gr

CrossMark

Abstract

We studied the production of neutron-rich nuclides in multinucleon transfer collisions of stable and radioactive beams (RIB) in the mass range $A \sim 40$–60. We first presented our experimental cross section data of projectile fragments from the reaction of ^{40}Ar(15 MeV/nucleon) with ^{64}Ni, ^{58}Ni and ^{27}Al. We then compared them with calculations based on either the deep-inelastic transfer model or the constrained molecular dynamics model, followed by the statistical multifragmentation model. An overall good agreement of the calculations with the experimental data is obtained. We continued with calculations of the reaction of ^{40}Ar (15 MeV/nucleon) with ^{238}U target and then with reactions of ^{48}Ca (15 MeV/nucleon) with ^{64}Ni and ^{238}U targets. In these reactions, very neutron-rich rare isotopes are produced with large cross sections. These nuclides, in turn, can be assumed to form RIB and interact with a subsequent target (preferably ^{238}U), leading to the production of extremely neutron-rich and even new isotopes (e.g. ^{60}Ca) in this mass range. We conclude that multinucleon transfer reactions with stable or RIB at energy around 15 MeV/ nucleon offer an effective route to access extremely neutron-rich rare isotopes for nuclear structure or reaction studies.

(Some figures may appear in colour only in the online journal)

1. Introduction

The study of the chart of the nuclides toward the astrophysical r-process path and the neutron drip-line continues to receive special attention by the nuclear physics community (see, e.g., [1–4]). Moreover, the efficient production of very neutron-rich nuclides constitutes a central issue in current and upcoming rare isotope beam facilities (see, e.g., [5–15]).

The production of neutron-rich nuclides traditionally follows three main routes: spallation, fission and projectile fragmentation [16]. Spallation is a standard mechanism to produce rare isotopes in ISOL-type facilities [17]. Projectile fission is very effective to produce neutron-rich light and heavy fission fragments (see, e.g., [18–20]). Finally, projectile fragmentation is a universal approach to access exotic nuclei at beam energies typically above 100 MeV/nucleon (see, e.g., [21–26]). We note that in projectile fragmentation, the most neutron-rich products are obtained by stripping the maximum possible number of protons (and a minimum number of neutrons).

To access even more neutron-rich isotopes, apart from proton stripping from the projectile, pickup of neutrons from the target may be necessary. Such a possibility is offered by reactions involving nucleon exchange at beam energies from the Coulomb barrier [27–30] to the Fermi energy (below 40 MeV/nucleon) [31, 32]. There is renewed interest in such reactions nowadays as evidenced by recent experimental (e.g. [33–37]) and theoretical (e.g. [38–43]) works. These efforts focus mainly on multinucleon transfer reactions near the Coulomb barrier. We note that in these reactions, the fragments emerge with low velocities and wide angular and ionic charge state distributions that may result in practical limitations in the efficient collection for the most neutron-rich products.

The reactions in the Fermi energy regime (i.e. 15–35 MeV/nucleon) combine the advantages of both low-energy (i.e., near the Coulomb barrier) and high-energy (i.e., above 100 MeV/nucleon) reactions. At this energy, the overlap of the neutron-rich surfaces of the projectile and the target may enhance the neutron excess of the resulting fragments whose relatively high velocities may lead to efficient in-flight collection and separation.

Our previous experimental studies of projectile fragments from 15 and 25 MeV/nucleon reactions of ^{86}Kr [31, 32, 44–46] indicated substantial production of neutron-rich fragments. Our recent article [47] elaborates on our current understanding of the reaction mechanism and our ability to describe it quantitatively with the phenomenological deep-inelastic transfer (DIT) model, as well as with the microscopic constrained molecular dynamics (CoMD) model. As already pointed out in our previous works, the multinucleon transfer approach in the energy regime of 15–25 MeV/nucleon offers the possibility of essentially adding neutrons (along with the usual stripping of protons) to a given stable (or radioactive) projectile via interaction with a neutron-rich target.

In this article, after a short overview of our previous experimental measurements with an ^{40}Ar (15 MeV/nucleon) beam, we present systematic calculations of the production cross sections based on the phenomenological DIT model or the microscopic CoMD model. The good description of the experimental results with both the microscopic CoMD code, as well as, with the phenomenological DIT code, suggest the possibility of using the present theoretical framework for the prediction of exotic nuclei employing radioactive beams (RIB) that

will soon be available in upcoming facilities. As examples, we present the DIT calculated production cross sections and rates of neutron-rich nuclei using RIB of ^{46}Ar and ^{54}Ca at 15 MeV/nucleon.

The structure of the paper is as follows. In section 2, we give a short description of the experimental methods and in section 3 an overview of the models used. In sections 4–6 we compare our calculations to data for the stable beams ^{40}Ar and ^{48}Ca. In sections 7 and 8 we present calculations with the RIB ^{46}Ar and ^{54}Ca. Then, in section 9 we give a discussion and summary. Finally, appendix A elaborates on the properties of the primary fragments and appendix B on the energy dependence of the production cross sections.

2. Brief description of the experimental data and apparatus

Experimental data on neutron rich nuclide production with a beam of ^{40}Ar (15 MeV/nucleon) were obtained at the Cyclotron Institute of Texas A&M University, in parallel to a series of measurements with a ^{86}Kr (15 MeV/nucleon) beam already published in [46]. A preliminary version of the ^{40}Ar data has already been presented in [48]. The experimental setup has been presented in detail in [46]. For completeness, we give a brief overview of the experimental methods here. A 15 MeV/nucleon ^{40}Ar^{9+} beam hit targets of ^{64}Ni, ^{58}Ni and ^{27}Al with thickness of 2 mg cm^{-2}. Projectile fragments were collected and identified using the MARS recoil separator applying the techniques developed and documented in [46]. The ^{40}Ar beam was send on the primary target location of MARS with an angle of 4° with respect to the optical axis of the separator and projectile fragments were collected in the polar angular range of 2.2°–5.5° (in a solid angle of $\Delta\Omega = 4.0$ msr). After interaction with the target, the fragments traversed a parallel-plate avalanche counter (PPAC) at the intermediate image location (for position, magnetic rigidity and START-time information) and then they were focused at the end of the separator passing through a second PPAC (for image-size and STOP-time information). Finally the fragments were collected in a 5×5 cm^2 ΔE–E Si detector telescope (with 60 and 1000 μm thickness, respectively). Following standard techniques of $B\rho$–ΔE–E– TOF (magnetic rigidity, energy-loss, residual energy and time-of-flight, respectively), the atomic number Z, the mass number A, the velocity and the ionic charge of the fragments were obtained on an event-by-event basis. Data were obtained in a series of successive magnetic rigidity settings of the spectrometer in the range 1.1–1.5 Tm. We note that this magnetic rigidity range did not fully cover the neutron-deficient side of the product distributions which extends down to 0.8 Tm according to our calculations. (The neutron-deficient isotopes with incomplete $B\rho$ coverage lie to the left of the thin solid lines in figures 1–3 and 6.)

In order to obtain total cross sections of the produced isotopes, we applied corrections to the measured yields for the limited angular coverage of the spectrometer, as performed in our previous work [46]. The corrections were based on simulations of the reactions using the DIT code (see below) followed by a de-excitation code [46]. We used the ratio of filtered to unfiltered calculated yields to correct the measured data (obtained in the limited angular acceptance of the spectrometer) and to extract the total production cross section for each isotope that we discuss in the following.

In figure 1 we present the extracted cross sections of the isotopes of elements $Z = 19$–12 for the three reactions studied: ^{40}Ar (15 MeV/nucleon) + ^{64}Ni, ^{58}Ni and ^{27}Al, represented by closed (black) circles, open (red) circles and open (blue) squares, respectively. We clearly observe enhanced production of neutron-rich isotopes with the more neutron-rich target of ^{64}Ni ($N/Z = 1.28$), followed by ^{58}Ni ($N/Z = 1.07$) and, finally, by ^{27}Al ($N/Z = 1.08$). Interestingly, few-neutron pickup nuclides are produced in all three reactions. These nuclides
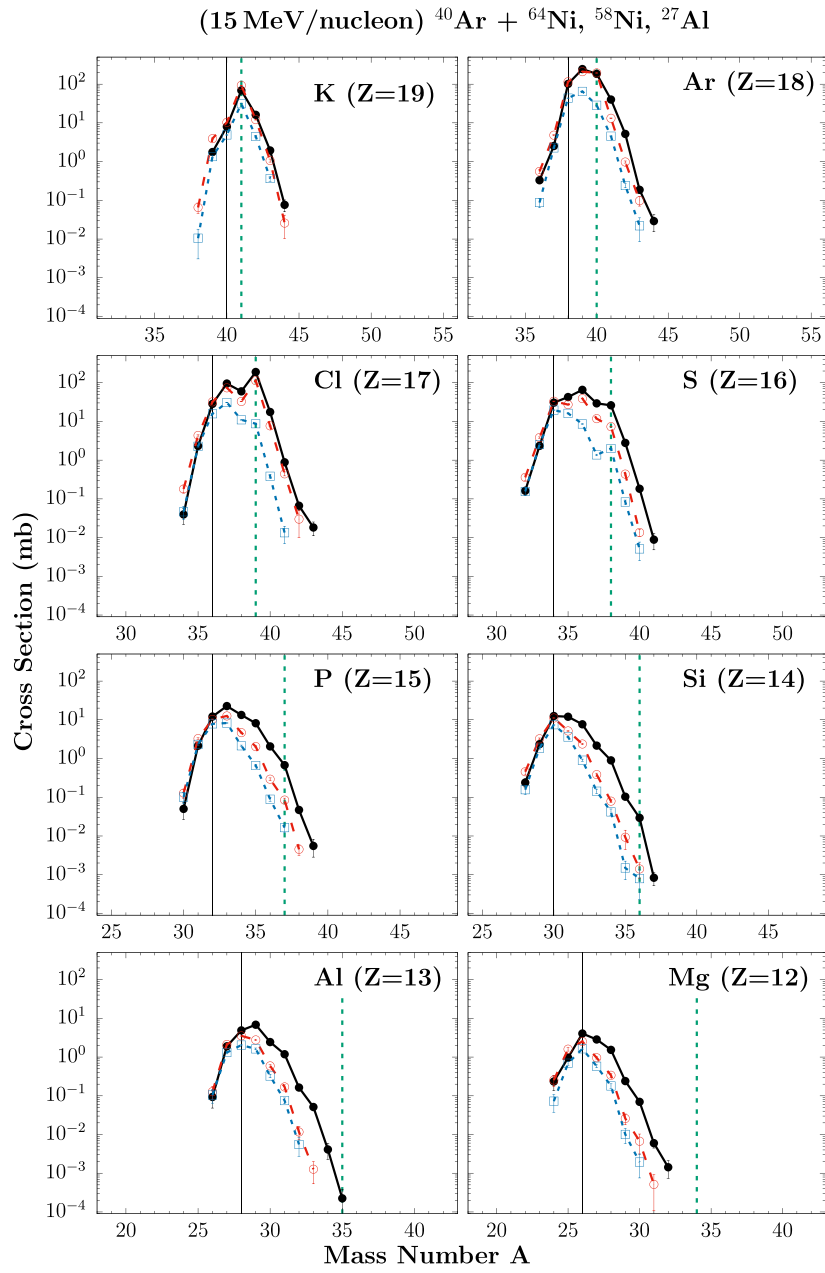
$(15\,\mathrm{MeV/nucleon})\ ^{40}\mathrm{Ar} + {}^{64}\mathrm{Ni},\ {}^{58}\mathrm{Ni},\ {}^{27}\mathrm{Al}$

Figure 1. Experimental mass distributions (cross sections) of the isotopes of elements $Z = 19$–12 for the three reactions measured: ^{40}Ar (15 MeV/nucleon) + ^{64}Ni, ^{58}Ni and ^{27}Al, represented by closed (black) circles, open (red) circles and open (blue) squares, respectively. Nuclides to the left of the thin solid lines are not fully covered by the magnetic rigidity range of the experiment (see text). Nuclides with a net pickup of neutrons from the target lie to the right of the dotted lines.

4

Figure 2. Comparison of calculated mass distributions (lines) of projectile fragments with $Z = 19$–12 from the reaction ^{40}Ar (15 MeV/nucleon) $+ {}^{64}$Ni with the experimental data (closed (black) circles, as in figure 1). The calculations are: DIT/ SMM (solid (red) line) and CoMD/SMM (dashed (blue) line). Nuclides to the left of the thin solid lines are not fully covered by the magnetic rigidity range of the experiment (see text). Nuclides with a net pickup of neutrons from the target lie to the right of the dotted lines.
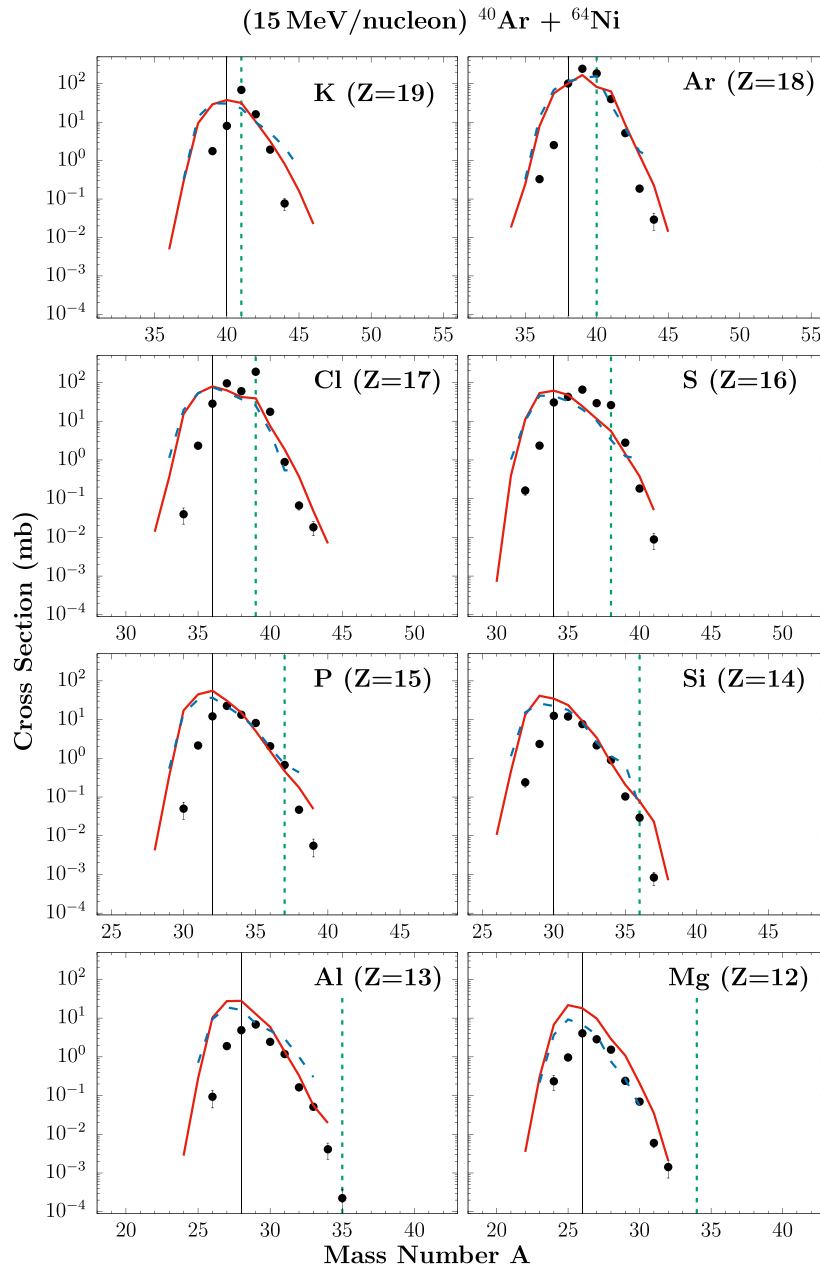
$(15\,\mathrm{MeV/nucleon})\ {}^{40}\mathrm{Ar} + {}^{64}\mathrm{Ni},\ {}^{238}\mathrm{U}$

Figure 3. DIT/SMM calculated mass distributions (cross sections) of projectile fragments with $Z = 19$–12 from the reaction ${}^{40}\mathrm{Ar}$ (15 MeV/nucleon) + ${}^{238}\mathrm{U}$ (dashed (blue) line) compared with those from ${}^{40}\mathrm{Ar}$ (15 MeV/nucleon) + ${}^{64}\mathrm{Ni}$ (solid (red) line) and the experimental data [closed (black) circles]. Nuclides to the left of the thin solid lines are not fully covered by the magnetic rigidity range of the experiment (see text). Nuclides with a net pickup of neutrons from the target lie 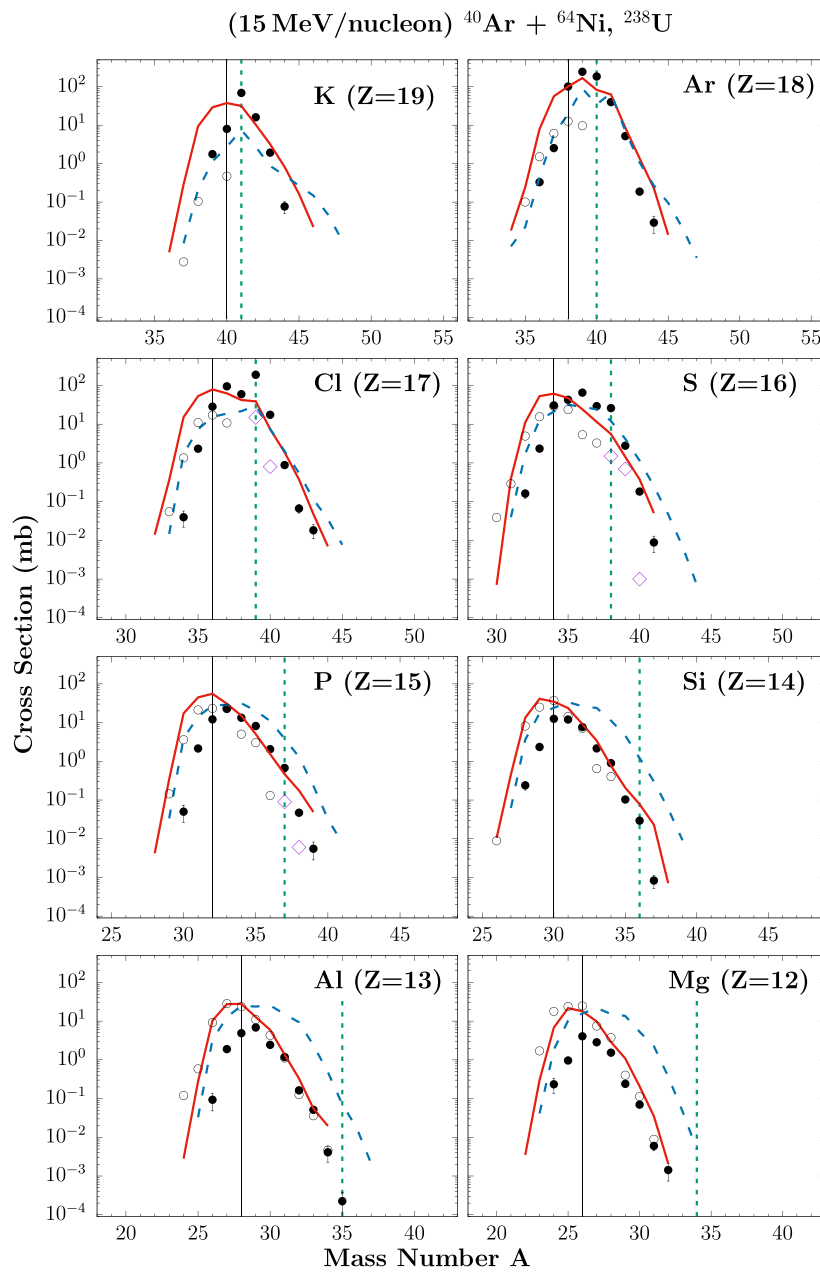to the right of the dotted lines. In addition, the projectile fragmentation data of [65] on ${}^{40}\mathrm{Ar}$ (94 MeV/nucleon) + ${}^{181}\mathrm{Ta}$ are presented by open circles and those of [66] of the same system at 57 MeV/nucleon by open diamonds.

6

lie to the right of the vertical dotted lines in figure 1 (and subsequent figures). As expected, the reaction with the most neutron-rich of the three targets leads to the highest production of these nuclides in the data. Especially for elements very close to the projectile, e.g. $Z = 19$–16, the neutron-pickup possibility provides a distinct advantage of these reactions in comparison to the well-established projectile fragmentation approach, in which the neutron pickup possibility is suppressed, as we will also discuss in the following.

3. Outline of the theoretical models

The calculations performed in this work are based on a two-stage Monte Carlo approach. The dynamical stage of the collision was described by two different models: first, we employed the phenomenological DIT model [49–51] simulating stochastic nucleon exchange in peripheral collisions. This model has been extensively employed to describe the N/Z, excitation energy, and kinematical properties of excited quasiprojectiles in a number of recent studies (e.g. [52] and references therein), including our work on rare isotope production below the Fermi energy, as referenced in the previous section.

We used the microscopic CoMD model [53–57] successfully used in studies of low- and medium-energy reaction dynamics. This code is based on the general approach of the quantum molecular dynamics models [58] describing the nucleons as localized Gaussian wave packets that interact via an effective nucleon–nucleon interaction. This interaction has a simplified Skyrme-like form corresponding to a nuclear-matter compressibility of $K = 200$ (soft equation-of-state) and also has several forms of the density dependence of the nucleon–nucleon symmetry potential. During the time evolution of the colliding system, a phase space constraint is imposed to restore the Pauli principle. As in our recent studies at 15 and 25 MeV/nucleon [47, 59], in this work we mainly employed a symmetry potential proportional to the density, (that we called the standard symmetry potential). We also performed calculations with a symmetry potential proportional to the square root of the density (soft symmetry potential), as well as with one proportional to the square of the density (hard symmetry potential). Both of them led to nearly similar results for the peripheral collisions involved in this study and are not shown in the paper. In the present CoMD calculations, the dynamical evolution of the system was stopped at $t = 300$ fm c^{-1} (10^{-21} s) [47].

After the dynamical stage that was simulated either by the DIT code or the CoMD code, the de-excitation stage of the reaction was described by the statistical code statistical multifragmentation model (SMM) of Botvina [60–63]. The code, first, generates thermally equilibrated partitions of hot fragments. These fragments are then propagated in their mutual Coulomb fields while undergoing statistical de-excitation. We note that for low excitation energy events ($E^* < 1$ MeV/nucleon) relevant to the production of very neutron-rich nuclei, the SMM code describes the de-excitation process as a sequence of emissions of neutrons and light charged particles using the Weisskopf–Ewing model of statistical evaporation [50, 51].

After this outline of the models, we briefly comment on the physical basis of the two models used to describe the dynamical stage. The DIT model is a phenomenological nucleon-exchange model with empirical parameters carefully chosen to describe peripheral reactions at the Fermi energy and below. On the other hand, the CoMD model is a fully microscopic (semiclassical) N-body model employing empirical interactions among the nucleons adjusted to describe the known static properties of nuclei (i.e., radii, masses, etc). As such, the code has essentially no adjustable parameters that depend on the reaction dynamics. Furthermore, in contrast to mean-field models, the CoMD approach naturally takes into account correlations

among nucleons that are important to describe observables involving fluctuations, as for example the nucleon exchange in peripheral heavy-ion collisions.

We mention that multinucleon transfer in reactions near the Coulomb barrier has been described by the fully quantal time-dependent Hartree–Fock approach (see, e.g., [39, 40] and references therein), which is, however not appropriate for energies well above the Coulomb barrier. Thus, the microscopic CoMD model offers an appropriate theoretical framework to describe the present reactions and may be reliably applied to situations where no experimental data are available, especially in reactions with neutron-rich rare isotope beams. However, due to the computer-intensive character of the CoMD calculations, in the present work we relied mainly on the DIT model for the calculation of very small cross sections, as we will discuss in the following sections.

Finally we mention that in this work, we focused our attention only to projectile fragments which are the products of interest for the study of the most exotic isotopes. Of course, our model framework can provide the corresponding information on the target fragments when needed for practical applications.

4. Reactions with the ^{40}Ar projectile at 15 MeV/nucleon

In this section, we first present comparisons of the calculated production cross sections of ^{40}Ar projectile fragments with our experimental data. Since our goal is toward the optimum production of neutron-rich isotopes, the comparisons will focus on the reaction of ^{40}Ar with the ^{64}Ni target. Similar comparisons were performed with the other two targets (resulting in equivalent quality of agreement) and are not reported in this paper.

In figure 2, we show the calculated mass distributions of projectile fragments with $Z = 19$–12 from the reaction ^{40}Ar (15 MeV/nucleon) + ^{64}Ni obtained by DIT/SMM (solid (red) line) and by CoMD/SMM (dotted (blue) line) and compare them with the experimental data (closed points) described above (figure 1). We observe that the results of the two models are almost identical and in good agreement with the experimental data, especially for isotopes close to the projectile ($Z = 19$–16). As mentioned in section 2, the discrepancy between the calculation and the experimental data on the neutron-deficient side is due to incomplete coverage of the magnetic rigidity in the experiment that resulted in loss or incomplete collection of the neutron-deficient nuclides. Moreover, the agreement of the DIT calculations with those with the microscopic CoMD model, as well as with the data gives us confidence in the use of the DIT code for further systematic study of reactions for which no experimental data exist at present.

In figure 3, we proceed to show the DIT/SMM calculations for the reaction of ^{40}Ar (15 MeV/nucleon) with the heavy and very neutron-rich ^{238}U ($N/Z = 1.59$) target (dashed (blue) line) along with the DIT/SMM calculations (solid (red) line) of ^{40}Ar + ^{64}Ni and the experimental data (closed points) that we already presented in figure 2. As we might expect, the heavy ^{238}U target leads to further enhanced production of neutron-rich isotopes, especially at the tails of the distributions, as compared to those with the ^{64}Ni target. For further comparison in figure 3, we also show the projectile fragmentation data of Notani [64, 65] for the reaction ^{40}Ar (94 MeV/nucleon) + ^{181}Ta (open circles). In these data we observe the absence of neutron-pickup nuclides. However, such products are reported in the fragmentation data of Zhang *et al* [66] with a beam of ^{40}Ar (57 MeV/nucleon) on ^{181}Ta (shown in figure 3 by open diamonds) and ^{9}Be targets, as well as the data of Kwan *et al* [67] for the same reactions at 140 MeV/nucleon. These pick-up products have cross sections lower by a factor of 10 or more compared to the present 15 MeV/nucleon reactions. This may be attributed to the short

contact time of the projectile with the target that prevents nucleon exchange, which takes place extensively in the lower energy (e.g. 15 MeV/nucleon) reactions.

Apart from fragmentation data, we compared our calculated cross sections from 15 MeV/nucleon ^{40}Ar + ^{238}U with the recent experimental data of Mijatovic *et al* [36] on 6.4 MeV/nucleon ^{40}Ar + ^{208}Pb. This comparison indicated that the most neutron-rich isotopes reported in [36] near and below the ^{40}Ar projectile have cross sections similar (within a factor of two) to our calculated cross sections for Ar+U at 15 MeV/nucleon. We also note that the lower energy reaction has a wider angular distribution compared to the 15 MeV/ nucleon reaction (see also figure 4 below), that may render the latter more efficient for the collection of the most exotic species. From the above comparisons and discussion, we understand that at the energy of the present study (15 MeV/nucleon), the reactions of choice are those with the neutron-rich target of ^{238}U, since they lead to especially enhanced production of the most neutron-rich isotopes.

It is interesting to note that the reaction with the ^{238}U target leads to substantially enhanced cross sections for neutron-rich nuclides far from the projectile, e.g. for Si, Al and Mg isotopes in figure 3. The cross sections for the most neutron-rich of these isotopes (e.g. ^{35}Al, ^{32}Mg) are more than two orders of magnitude larger than those obtained with the ^{64}Ni target in our reactions at 15 MeV/nucleon (or with the projectile fragmentation reactions). This enhanced production has been experimentally observed in our previous work with ^{86}Kr(25 MeV/nucleon) + ^{208}Pb and successfully described with the DIT/SMM model framework mainly as asymmetric binary decay of extremely neutron-rich quasiprojectiles [62, 63].

5. Angular distributions of projectile fragments from ^{40}Ar reactions at 15 MeV/ nucleon

To understand the angular spread of the projectile fragments from the reactions of the ^{40}Ar projectile at 15 MeV/nucleon, in figure 4(a) we show the DIT/SMM-calculated angular distributions for the ^{40}Ar + ^{64}Ni system for which the grazing angle is 7.0°. The successive contours (from the interior) represent a decrease in the cross section by a factor of two. The pair of horizontal full lines represent the polar angular acceptance of the MARS spectrometer in the experimental setup of [46] (section 2). The pair of horizontal dashed lines indicate the angular acceptance of the KOBRA separator [68], that is a representative large-acceptance separator designed for rare-isotope production in the upcoming RIB facility RISP [14]. In the KOBRA setup, the beam is assumed to hit the primary target at an angle of 5° and fragments are collected in the polar angular range of 0°–10° in a solid angle of $\Delta\Omega = 50$ msr.

From the figure, we can appreciate the effect of the limited angular acceptance of a medium acceptance separator like MARS. Our simulations indicate that a fraction of ∼5% (taking into account the azimuthal acceptance also) of the produced near-projectile fragments falls in the angular acceptance of the MARS spectrometer. However, with an advanced large-acceptance separator like KOBRA, a larger fraction of fragments (approaching 50%–80%) can be collected, provided that the primary beam is sent on the target at the appropriate angle (chosen to be near the grazing angle of the reaction).

In figure 4(b), we show the angular distributions for the reaction of ^{40}Ar (15 MeV/ nucleon) with the heavier target ^{238}U. The grazing angle for this system is 20°. We clearly see that the angular distribution of the near-projectile fragments is much broader, making the efficient collection of the fragments especially challenging. For this reaction, the optimal angle to send the beam on the target (or, equivalently, to rotate a large acceptance
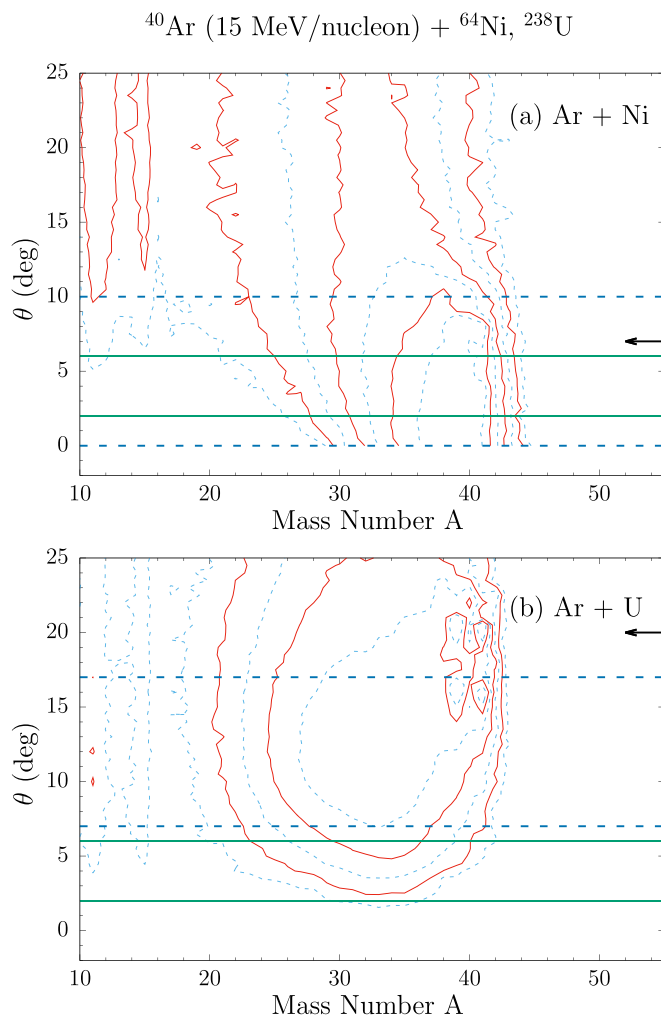
^{40}Ar (15 MeV/nucleon) + ^{64}Ni, ^{238}U

Figure 4. (a) DIT/SMM calculated mass-resolved angular distributions of projectile fragments from the reaction ^{40}Ar (15 MeV/nucleon) + ^{64}Ni. The successive contours (starting from the innermost) represent a decrease in the yield by a factor of two. The solid (green) lines represent the polar angular acceptance of the MARS spectrometer, and the dashed (blue) lines the optimum angular acceptance of the KOBRA spectrometer for this reaction. The arrow indicates the grazing angle of the Ar + Ni reaction (in the lab system). (b) As in panel (a), but for the reaction ^{40}Ar (15 MeV/ nucleon) + ^{238}U. In this case, the angular acceptance of KOBRA corresponds to the maximum angle of the beam on the target (see text).

spectrometer) is 18°, thus, collecting the fragments in the polar angular range of 13°–23°. With a solid angle acceptance of $\Delta\Omega = 50$ msr, the collection efficiency can reach 20%– 30%. We note, however, that the current design of the KOBRA spectrometer allows the beam to be sent on the target with a maximum angle of 12°, in which case the collection efficiency may be lower by a factor of 2.

From a practical standpoint, the use of the lighter target is preferable, as it leads to narrower angular distributions and thus larger collection efficiency, which may be desirable

for certain applications. However, the enhanced production of the most exotic nuclides obtained with the ^{238}U target, encourages the development of approaches for the efficient collection of fragments from these reactions. In closing, we mention that our simulations may allow event-by-event tracking of the products through the beam-optical elements of the separator allowing the determination of rates for production and separation of desired neutron-rich nuclides.

6. Reactions with a ^{48}Ca projectile at 15 MeV/nucleon

As discussed in section 4 in relation to figures 2 and 3, the cross section calculations for the ^{40}Ar (15 MeV/nucleon) projectile are in fair agreement with the experimental data giving us confidence on the reliability of the models used. Moreover, the calculations of the reactions with ^{238}U showed us that this target offers the possibility of enhanced production of the most neutron-rich nuclides. Motivated by these results, we proceeded to perform calculations with the most neutron-rich stable beam in this mass range, namely ^{48}Ca at 15 MeV/nucleon for which there are no experimental data at present.

In figure 5, we show our DIT/SMM calculations for the reactions ^{48}Ca (15 MeV/ nucleon) + ^{64}Ni (solid (red) line) and ^{48}Ca (15 MeV/nucleon) + ^{238}U (dashed (blue) line). In addition, we present the projectile fragmentation data of Mocko *et al* [69, 70] for the reaction ^{48}Ca (140 MeV/nucleon) + ^{181}Ta (open circles).

At first, observations similar to those for figure 3 pertain here. We see that both the ^{48}Ca + ^{64}Ni and ^{48}Ca + ^{238}U reactions at 15 MeV/nucleon lead to substantial yields of neutron pickup products with the latter reaction offering higher yields. Interestingly, the fragmentation of ^{48}Ca at 140 MeV/nucleon with the heavy neutron-rich ^{181}Ta ($N/Z = 1.48$) target leads to the production of neutron pickup products with cross sections nearly similar to those calculated for the ^{48}Ca(15 MeV/nucleon) + ^{64}Ni reaction. (We mention that such nuclides are also produced in the fragmentation of ^{48}Ca (140 MeV/nucleon) on the ^{9}Be target with cross ections lower by at least a factor of 10.) It would be interesting to describe theoretically the neutron pickup products from typical fragmentation reactions on heavy targets (e.g. ^{181}Ta, ^{208}Pb, ^{238}U) at the energy of $\sim$100 MeV/nucleon, which is at the lower limit of the typical projectile fragmentation mechanism [71, 72]. In the near future, we plan to undertake such a project using our theoretical model framework. In regards to higher energy projectile fragmentation, for completeness, we report the work of Suzuki *et al* [73] on ^{48}Ca (345 MeV/nucleon) + ^{9}Be, in which no pickup products were reported. The most neutron-rich isotopes observed were proton-removal products with cross sections similar to those of the 140 MeV/nucleon data of Mocko *et al* [69].

7. Reactions with the RIB of ^{46}Ar and ^{54}Ca at 15 MeV/nucleon

After the above calculations and comparisons on reactions with the stable beams of ^{40}Ar and ^{48}Ca, we continue our study with reactions involving the neutron-rich RIB of ^{46}Ar (figures 6 and 7) and ^{54}Ca (figure 8). We chose these neutron-rich projectiles as representative examples of RIB in this mass range, having six more neutrons than their stable counterparts ^{40}Ar and ^{48}Ca, respectively.

In figure 6, we show the DIT/SMM calculations for the RIB reaction ^{46}Ar (15 MeV/ nucleon) + ^{64}Ni (dashed (blue) line) compared with the calculation for the stable-beam reaction ^{40}Ar (15 MeV/nucleon) + ^{64}Ni and our experimental data (closed points) as in figure 2. We observe that the RIB leads to an isotope distribution with a neutron-rich side
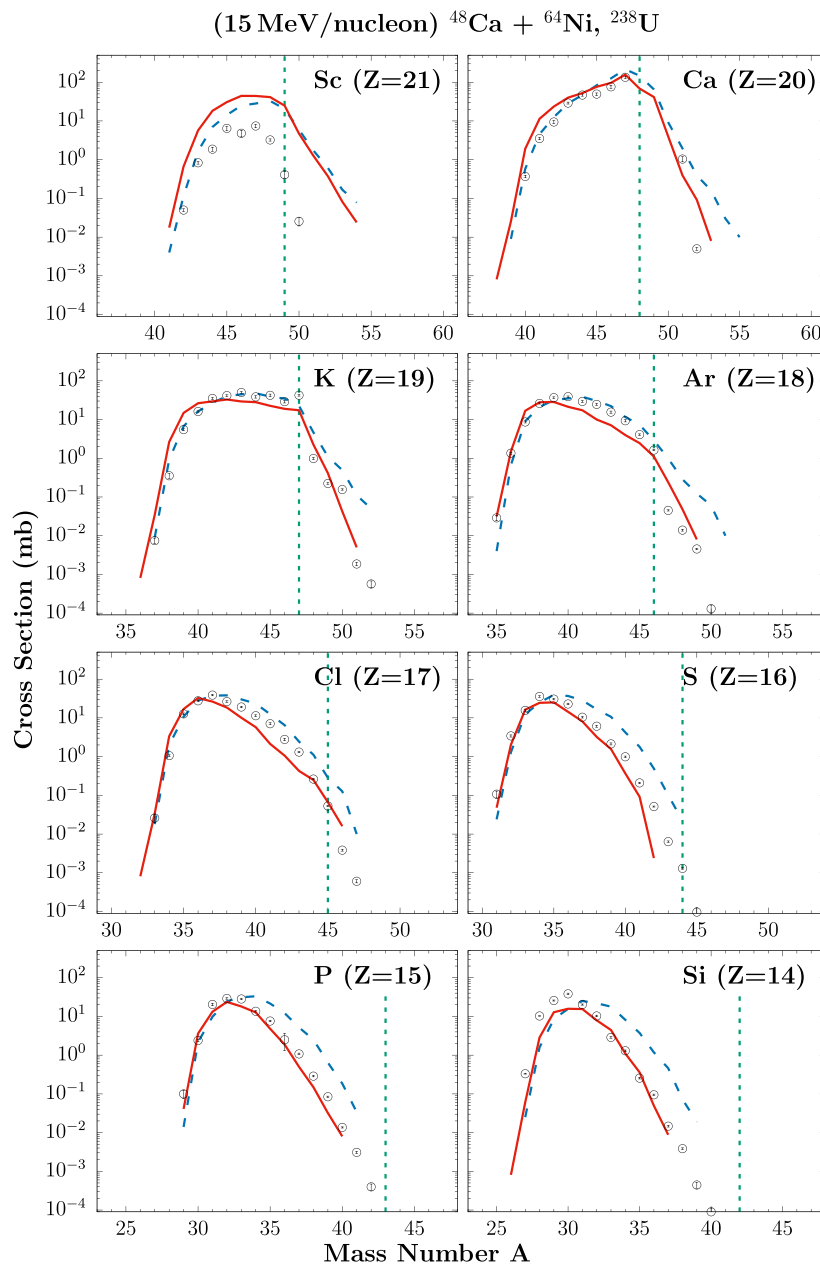
Figure 5. DIT/SMM calculated mass distributions (cross sections) of projectile fragments with $Z = 21$–14 from the reactions ^{48}Ca (15 MeV/nucleon) + ^{64}Ni (solid (red) line) and ^{48}Ca (15 MeV/nucleon) + ^{238}U (dashed (blue) line) compared with the projectile fragmentation data of [69, 70] on ^{48}Ca (140 MeV/nucleon) + ^{181}Ta [open (black) circles]. Nuclides with a net pickup of neutrons from the target lie to the right of the dotted lines.
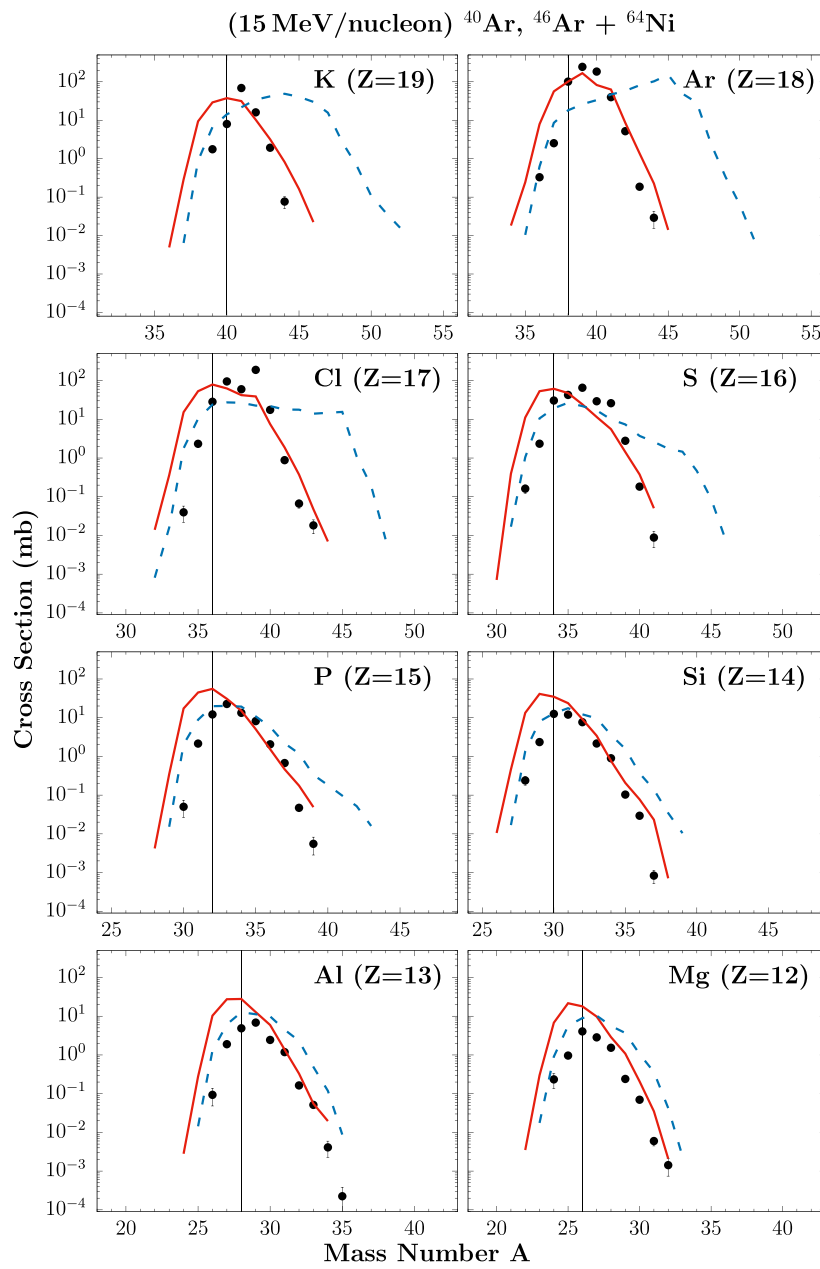
Figure 6. DIT/SMM calculated mass distributions (cross sections) of projectile fragments with Z = 19–12 from the radioactive-beam reaction ^{46}Ar (15 MeV/nucleon) + ^{64}Ni (dashed (blue) line) compared with the stable-beam reaction ^{40}Ar (15 MeV/nucleon) + ^{64}Ni (solid (red) line) and the experimental data [closed (black) circles]. As in figures 1–3, nuclides to the left of the thin solid lines are not fully covered by the magnetic rigidity range of our 15 MeV/nucleon experiment.
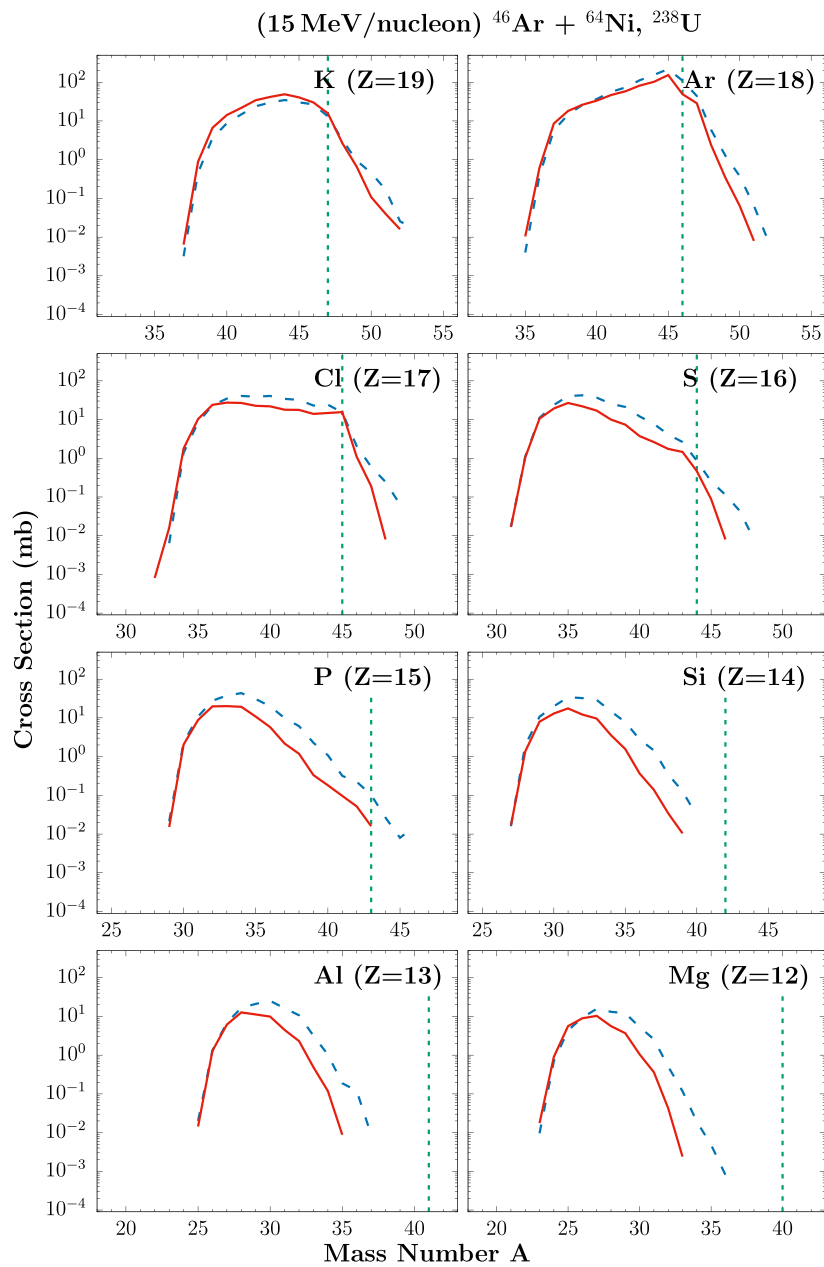
Figure 7. DIT/SMM calculated mass distributions (cross sections) of projectile fragments with $Z = 19$–12 from the reaction of a radioactive-beam of ^{46}Ar (15 MeV/nucleon) on ^{64}Ni (solid (red) line) and ^{238}U (dashed (blue) line). Nuclides with a net pickup of neutrons from the target lie to the right of the dotted lines.

displaced by several neutrons (nearly six for near-projectile elements) compared with that of the stable beam. We also notice that the enhanced production of the neutron-rich isotopes offered by the RIB diminishes substantially for products further away from the projectile (see
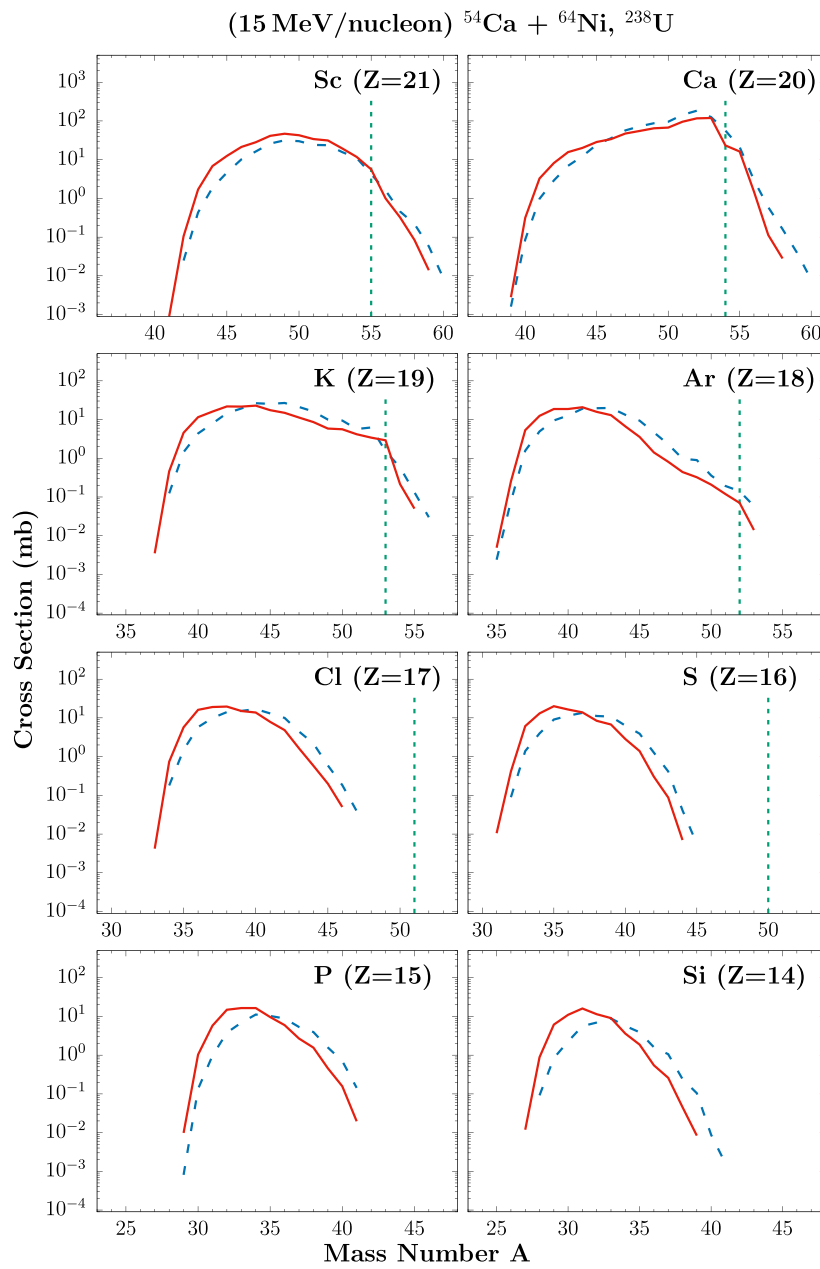
Figure 8. DIT/SMM calculated mass distributions (cross sections) of projectile fragments with $Z = 21$–14 from the reaction of a radioactive-beam of ^{54}Ca (15 MeV/nucleon) on ^{64}Ni (solid (red) line) and ^{238}U (dashed (blue) line). Nuclides with a net pickup of neutrons from the target lie to the right of the dotted lines.
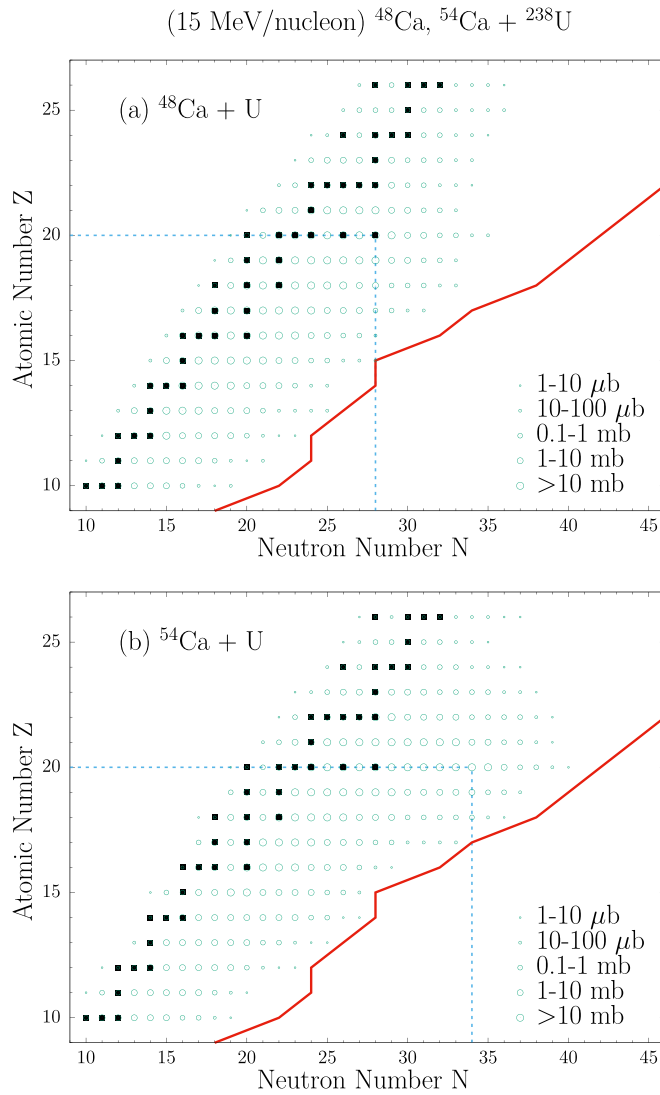
Figure 9. Representation on the *Z–N* plane of DIT/SMM calculated production cross sections of projectile fragments from 15 MeV/nucleon reactions of (a) the stable beam ^{48}Ca with ^{238}U, and (b) the radioactive-beam ^{54}Ca with ^{238}U. The cross section ranges are shown by open circles according to the key. The closed squares show the stable isotopes. The solid (red) line represents the expected location of the neutron drip line according to [74]. The horizontal and vertical dotted line segments indicate the location of the projectiles.

also [47], figure 9). In figure 7, we show the DIT/SMM calculations for the reactions of ^{46}Ar (15 MeV/nucleon) with ^{64}Ni (solid (red) line) and ^{238}U (dashed (blue) line). As expected, we notice that the ^{238}U target leads to enhanced neutron-rich isotope production, compared with the ^{64}Ni target, especially at the tails of the distributions for near-projectile elements.

Continuing our discussion with the ^{54}Ca RIB, in figure 8 we show the DIT/SMM calculations for the reaction ^{54}Ca (15 MeV/nucleon) + ^{64}Ni (solid (red) line) and ^{238}U

Table 1. Calculated cross sections (with DIT/SMM) and rates of neutron-rich isotopes from the stable-beam reaction ^{48}Ca (15 MeV/nucleon) + ^{238}U. For the rates, the beam intensity is assumed to be 500 pnA (3×10^{12} particles s^{-1}) and the target thickness 20 mg cm^{-2}. Isotope halflives are taken from [77, 74].

Rare isotope	$t_{1/2}$ (s)	Reaction channel	Cross section (mb)	Rates (s^{-1})
^{54}Ca	0.09	$-0p + 6n$	0.030	4.6×10^3
^{46}Ar	8.4	$-2p + 0n$	2.9	4.4×10^5
^{55}Sc	0.09	$+1p + 6n$	0.050	7.8×10^3
^{52}K	0.10	$-1p + 5n$	0.050	7.8×10^3

Table 2. Calculated cross sections (with DIT/SMM) and rates of neutron-rich isotopes from the radioactive-beam reaction ^{46}Ar (15 MeV/nucleon) + ^{238}U. For the rates, the beam intensity is assumed to be 4.4×10^5 particles s^{-1} and the target thickness 20 mg cm^{-2}. Isotope halflives are taken from [77, 74].

Rare isotope	$t_{1/2}$ (ms)	Reaction channel	Cross section (mb)	Rates (h^{-1})
^{51}Ar	24	$-0p + 5n$	0.064	5.0
^{52}Ar	16	$-0p + 6n$	0.008	0.6
^{48}Cl	39	$-1p + 3n$	0.24	18
^{49}Cl	28	$-1p + 4n$	0.064	5.0

(dashed (blue) line). Observations similar to those of figure 7 pertain here. Moreover, as we showed in figure 6 for ^{40}Ar/^{46}Ar and in comparison with figure 5, we note that the ^{54}Ca RIB results in an isotope distribution with a neutron-rich side displaced to the right compared with that of the ^{48}Ca stable beam. Finally, we notice that extremely neutron-rich and even new isotopes toward ^{60}Ca are produced in the RIB reaction ^{54}Ca + ^{238}U target.

8. Isotope production rates

A comprehensive presentation on the *Z–N* plane of the DIT/SMM calculated production cross sections of projectile fragments from the 15 MeV/nucleon reactions ^{48}Ca + ^{238}U and ^{54}Ca + ^{238}U is given in figure 9. In this figure, stable isotopes are represented by closed squares, whereas fragments obtained by the respective reactions are given by the open circles (with sizes corresponding to cross section ranges according to the figure key). The solid (red) line gives the expected location of the neutron drip line as calculated in [74]. In the figure, we clearly observe that the neutron pickup products from the radioactive beam reaction (figure 9(b)) extend toward the region of the neutron drip line near ^{62}Ca.

We now proceed to a discussion of the production rates of some representative neutron-rich rare isotopes. In table 1, we show the DIT/SMM calculated cross sections and the predicted production rates of some isotopes from the reaction ^{48}Ca (15 MeV/nucleon) + ^{238}U. We assume a beam intensity of 500 particle nA (3×10^{12} particles s^{-1}) and a target thickness of 20 mg cm^{-2}.

Subsequently, in table 2, we show the predicted cross sections and production rates of several isotopes from the reaction of a radioactive beam of ^{46}Ar (15 MeV/nucleon) with ^{238}U. In this case, we assumed that the beam intensity is equal to the production rate of ^{46}Ar from the reaction ^{48}Ca (15 MeV/nucleon) + ^{238}U (table 1) and that the target thickness is again

Table 3. Calculated cross sections (with DIT/SMM) and rates of neutron-rich isotopes from the radioactive-beam reaction ^{54}Ca (15 MeV/nucleon) + ^{238}U. For the rates, the beam intensity is assumed to be 4.6×10^3 particles s^{-1} and the target thickness 20 mg cm^{-2}. Isotope halflives are taken from [77, 74]. (Theoretical estimates for new nuclides are marked with an asterisk.)

Rare isotope	$t_{1/2}$ (ms)	Reaction channel	Cross section (mb)	Rates (d^{-1})
^{57}Ca	7	$-0p + 3n$	0.60	12
^{58}Ca	12	$-0p + 4n$	0.16	3.2
^{59}Ca	6*	$-0p + 5n$	0.040	0.80
^{60}Ca	4*	$-0p + 6n$	0.008	0.16
^{54}K	10	$-1p + 1n$	0.57	11
^{55}K	4	$-1p + 2n$	0.13	2.6

20 mg cm^{-2}. We see that very exotic nuclei such as ^{52}Ar and ^{49}Cl can be produced with rates that may allow spectroscopic studies.

Finally, in table 3, we show the predicted cross sections and production rates of nuclides from the reaction of a radioactive beam of ^{54}Ca (15 MeV/nucleon) with ^{238}U. As before, we assumed a beam intensity equal to the production rate of ^{54}Ca from the reaction ^{48}Ca (15 MeV/nucleon) + ^{238}U (table 1) and a target thickness of 20 mg cm^{-2}. We notice that relatively low but 'usable' rates of extremely rare and even new isotopes, like ^{59}Ca ($\sim$1 per day) and ^{60}Ca ($\sim$1 per week) can be produced that may allow to obtain identification and basic spectroscopic information for such nuclides.

9. Discussion and plans

We conclude the present study, first, with some comments on the model approaches used in this work. The successful description of the reactions with the CoMD model used in the dynamical stage is especially valuable due to the predictive power of the microscopic many-body approach that is free of ad hoc assumptions on the reaction dynamics (as also seen in our recent works [19, 47, 57]). We saw that the two-stage CoMD/SMM approach provided good results in comparison with the experimental data. Nonetheless, we remind that it is very computer intensive due to the N-body CoMD stage of the calculation [47], that limited the extensive application in this work. On the contrary, the phenomenological DIT/SMM approach, providing results in overall agreement with the microscopic CoMD/SMM approach, is rather fast. For this reason we used it extensively in this study to estimate cross sections of very neutron-rich products. Moreover, this approach can be practical for the design of RIB experiments based on the present reactions.

As a continuation of the present work, we plan to perform systematic CoMD calculations toward the region of very low cross sections and compare them with the corresponding DIT results. Furthermore, we plan to continue the systematic calculation efforts with RIB that are expected from upcoming RIB facilities in the energy range of 10–25 MeV/nucleon. Concerning the choice of energy, our calculations, presented in the appendix, suggest that the energy of 15 MeV/nucleon is a reasonable choice for the efficient production of very neutron-rich isotopes close to the projectile. This conclusion is also in agreement with our previous experimental [46] and theoretical [47] work. Since our calculations are complete event-by-event simulations, they allow the systematic study of velocity distributions, angular distributions and ionic charge state distributions of the projectile fragments. This information can

form the basis of beam optics simulations of large acceptance separators and can contribute to the optimization of the separation and identification of the exotic neutron-rich nuclides.

In the near future, apart from systematic RIB calculations in the mass range 40–60, we plan to perform detailed measurements of projectile fragments from ^{48}Ca and ^{70}Zn beams at 10–15 MeV/nucleon (a) at Texas A&M with the MARS recoil separator [45, 46] and (b) at LNS/INFN with the MAGNEX large-acceptance spectrometer [75]. We expect that these measurements will provide a further detailed testing ground for our models, and will offer access to very neutron-rich nuclei for a broad range of studies. These studies may include measurements of secondary reactions, in-beam spectroscopy of selected products, decay measurements and further search for new isotopes or new isomers. In parallel, these efforts will provide experience and preparation for future plans at upcoming large-acceptance separator facilities (e.g. KOBRA [68], ISLA [76]).

10. Summary and conclusions

In this article we present our recent efforts toward systematic studies of the production of neutron-rich rare isotopes with heavy-ion beams in the energy range of 15–25 MeV/nucleon. We studied the production of neutron-rich projectile-like isotopes in multinucleon transfer collisions of stable and RIB in the mass range $A \sim 40$–60. We first presented our experimental cross section data on ^{40}Ar(15 MeV/nucleon) $+$ ^{64}Ni, ^{58}Ni and ^{27}Al and compared them with calculations. The calculations are based on two models: the phenomenological DIT model and the microscopic CoMD model employed to describe the dynamical stage of the collision. De-excitation of the resulting projectile-like fragments is performed with the statistical SMM. An overall good agreement of the calculations with the experimental data is obtained. We also performed calculations of the reaction of ^{40}Ar (15 MeV/nucleon) projectile with the heavy neutron-rich target of ^{238}U. We then continued with the reactions of the neutron-rich beam of ^{48}Ca (15 MeV/nucleon) with targets of ^{64}Ni and ^{238}U. In these reactions, we observed that neutron-rich rare isotopes with substantial cross sections can be produced which, in turn, may be assumed to form RIB and interact with a subsequent target, preferably ^{238}U, resulting in extremely neutron-rich and even new isotopes (e.g. ^{60}Ca) in this mass range. We conclude that multinucleon transfer reactions with stable or RIB at the energy of around 15 MeV/nucleon constitute a novel and competitive route to access extremely neutron-rich rare isotopes that may open up exciting nuclear research opportunities in current or upcoming rare isotope beam facilities.

Acknowledgments

$$^{40}\text{Ar}(15\text{MeV/nucleon}) + {}^{64}\text{Ni}, {}^{238}\text{U}$$
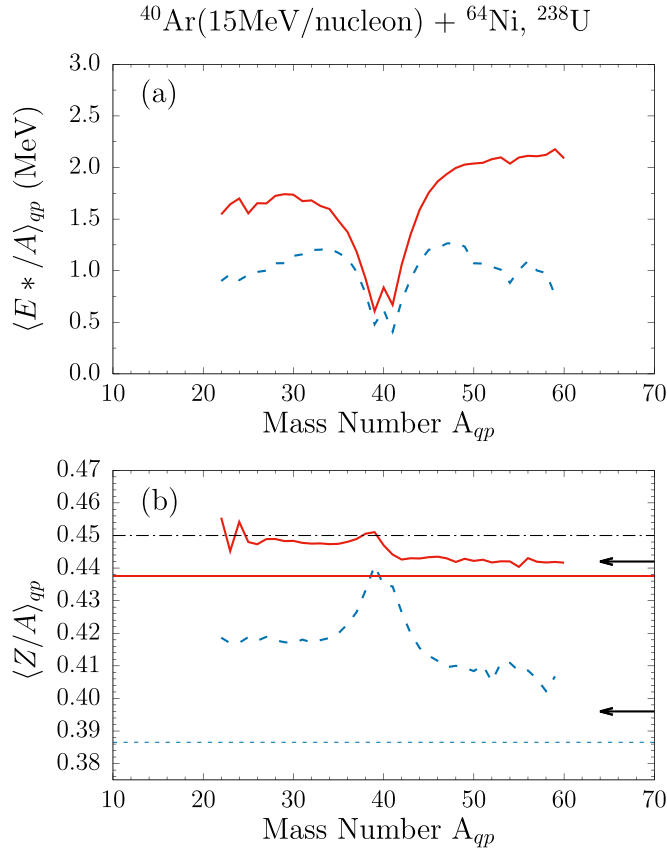

Figure A1. DIT calculated properties of quasiprojectiles. (a) Average excitation energy per nucleon E^*/A versus mass A of quasiprojectiles from the reactions ^{40}Ar (15 MeV/ nucleon) + ^{64}Ni (solid (red) line) and ^{40}Ar (15 MeV/nucleon) + ^{238}U [dotted (blue) line]. (b) Average Z/A versus A of quasiprojectiles. Lines are as in panel (a). The horizontal dashed–dotted line indicates the Z/A of the ^{40}Ar projectile. The horizontal full and dashed lines indicate the Z/A of the ^{64}Ni and ^{238}U target nuclei, respectively. The upper and lower arrows indicate the Z/A values corresponding to full N/Z equilibration for the ^{40}Ar + ^{64}Ni and ^{40}Ar + ^{238}U systems, respectively.

Appendix A. Properties of quasiprojectiles

In this appendix, we present some properties of the primary fragments (quasiprojectiles) from the 15 MeV/nucleon ^{40}Ar induced reactions on ^{64}Ni and ^{238}U. The calculations are with the DIT model. Similar results have been obtained with the CoMD model and are not shown here. We mention that in our previous work [52] on 15 and 25 MeV/nucleon peripheral heavy-ion collisions, we studied the relation of excitation energy and N/Z transport with respect to the degree of dissipation expressed by the total kinetic energy loss (TKEL) in the collision.

In figure A1(a), we show the average excitation energy per nucleon E^*/A as a function of the quasiprojectile mass for the reactions ^{40}Ar (15 MeV/nucleon) + ^{64}Ni (solid (red) line) and
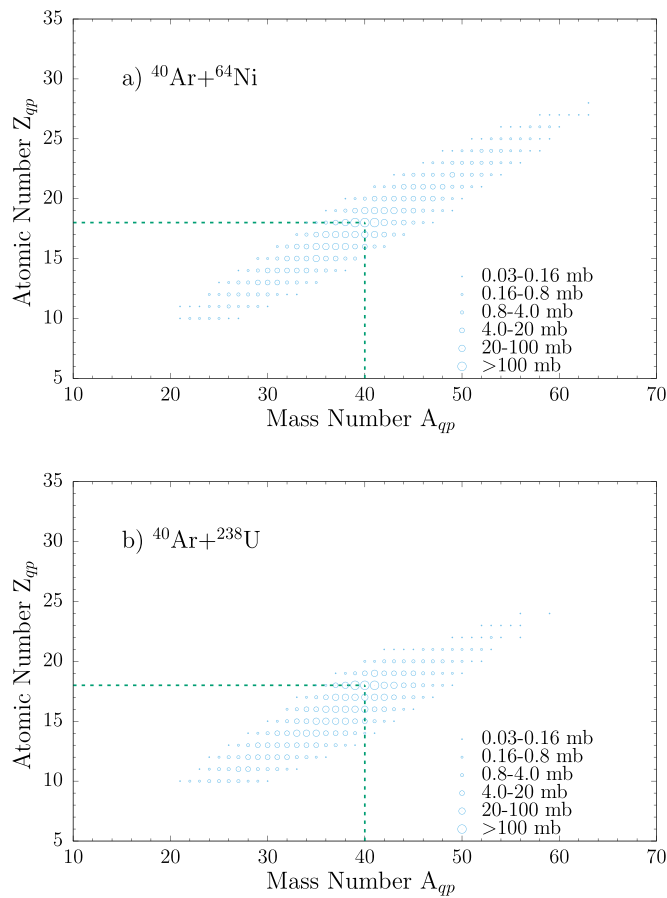
Figure A2. Representation of DIT calculated cross sections of quasiprojectiles from the 15 MeV/nucleon reactions ^{40}Ar + ^{64}Ni (a) and ^{40}Ar + ^{238}U (b) on the *Z–A* plane. The cross section ranges are shown by open circles according to the key. The lines indicate the location of the projectile nucleus ^{40}Ar.

^{40}Ar (15 MeV/nucleon) + ^{238}U (dashed (blue) line). We observe relatively low excitation energies for the quasiprojectiles in the region near $A = 40$ attributed to peripheral collisions with limited interaction between the projectile and the target. On the contrary, in higher or lower masses, progressively higher excitation energies are observed being higher for the reaction ^{40}Ar + ^{64}Ni than for ^{40}Ar + ^{238}U. This difference may be related to the fact that in peripheral and semiperipheral collisions, the mechanism responsible for energy dissipation is the exchange of nucleons. For the most peripheral collisions, the dissipated energy is nearly equally distributed to the reaction partners, whereas for more central events the excitation energy is divided in proportion to the mass of the reaction partners (thermal division). In the latter case, for a given TKEL, the light partner of a very asymmetric system like Ar + U may acquire lower excitation energy compared to the case of a more symmetric system like Ar + Ni.

In figure A1(b), we show the average proton fraction Z/A as a function of the quasi-projectile mass from the 15 MeV/nucleon reactions ^{40}Ar + ^{64}Ni (solid (red) line) and ^{40}Ar + ^{238}U (dashed (blue) line). The horizontal lines indicate the Z/A of ^{40}Ar, ^{64}Ni and ^{238}U (from higher to lower, respectively), whereas the arrows mark the Z/A values of fully N/Z equilibrated systems of ^{40}Ar + ^{64}Ni (upper arrow) and ^{40}Ar + ^{238}U (lower arrow). We observe that the Z/A for near-projectile primary fragments is, as expected, close to that of the projectile, whereas for those further away the Z/A departs from that of the projectile to values toward N/Z equilibration.

Furthermore, in figure A2, we give an outline of the distributions of the primary projectile products on the Z–A plane for ^{40}Ar + ^{64}Ni and ^{40}Ar + ^{238}U reactions. The cross section ranges are shown by the open circles according to the figure key, whereas the lines indicate the location of the projectile nucleus. From the figure we see that the distributions of the ^{40}Ar + ^{238}U reaction are wider than those of the ^{40}Ar + ^{64}Ni reaction, whereas the latter leads to a more extended region of trans-projectile elements as compared to the former. Combining this observation with figure A1(a), we understand that quasiprojectiles further in mass from the projectile are expected to be highly excited and decay via neutron or charged particle evaporation.

From the investigation of the excitation energy of the primary products, we find that the most neutron-rich isotopes are produced from quasiprojectiles with $E^*/A \sim 0.2$–0.5 MeV (i.e. with $E^* \sim 10$–30 MeV for the mass range $A = 50$–60) and, thus, they de-excite mostly via evaporation of 1–2 neutrons. This is the case of the primary products in figure A2 that lie at the right edge of the distributions and result, after neutron evaporation, to the final neutron-rich products whose cross sections were systematically analyzed in the preceding sections of this article.

Appendix B. Energy dependence of production cross sections

Finally, in this appendix, we examine the dependence of the cross sections of the neutron-rich products on the projectile energy. We consider the stable-beam reaction of ^{48}Ca with the ^{238}U target and performed DIT/SMM calculations at beam energies of 10, 15 and 25 MeV/nucleon. The results are presented in figure B1 by dashed (blue), solid (black) and dotted (red) lines, respectively. We observe that on the neutron-rich side, the reactions at the lower two energies, 10 and 15 MeV/nucleon, lead to nearly similar cross sections which are higher than those of the reaction at 25 MeV/nucleon. On the neutron-deficient side, the distributions of the 15 and 25 MeV/nucleon reactions are similar, indicating a possible similarity of the excitation energies of the quasiprojectiles leading to these isotopes. At 10 MeV/nucleon, the neutron-deficient nuclide cross sections are lower as a result of lower excitation energies reached in this reaction compared to the higher energy ones. The above comparisons lead us to the conclusion that the beam energy of 15 MeV/nucleon is a reasonable choice for the efficient production of the most neutron-rich nuclides in these multinucleon transfer reactions.
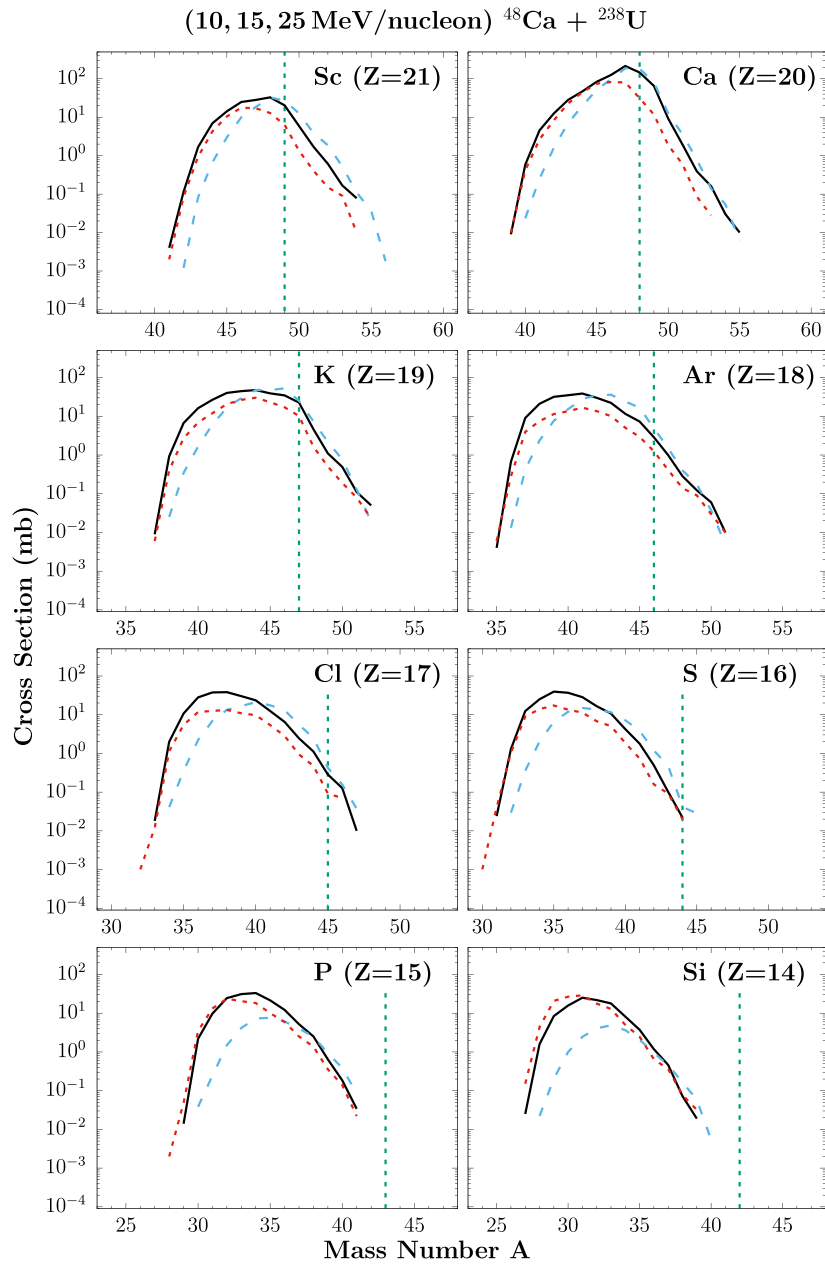
Figure B1. Energy dependence of DIT/SMM calculated mass distributions of projectile fragments with $Z = 21$–14 from the reaction of a ^{48}Ca beam with a ^{238}U target at energies of 10, 15 and 25 MeV/nucleon represented by dashed (blue), solid (black) and dotted (red) lines respectively. Nuclides with a net pickup of neutrons from the target lie to the right of the dotted lines.

ORCID iDs

G A Souliotis ⓘ https://orcid.org/0000-0002-0751-2063

References

[1] Utama R and Piekarewicz J 2017 *Phys. Rev.* C **96** 044308
[2] Afanasjev A V, Agbemava S E, Ray D and Ring P 2015 *Phys. Rev.* C **91** 014324
[3] Gade A *et al* 2015 *Eur. Phys. J.* A **51** 118
[4] Erler J *et al* 2011 *Nature* **486** 509
[5] Geesaman D F, Gelbke C K, Janssens R V F and Sherrill B M 2006 *Annu. Rev. Nucl. Part. Sci.* **56** 53
[6] FRIB main page: www.frib.msu.edu
[7] GANIL main page: www.ganil.fr
[8] GSI main page: www.gsi.de
[9] RIBF main page: www.rarf.riken.go.jp/Eng/facilities/RIBF.html
[10] ATLAS main page: www.phy.anl.gov/atlas/facility/index.html
[11] ISOLDE main page: home.cern/about/experiments/isolde
[12] SPES main page: www.lnl.infn.it/~spes_target
[13] EURISOL main page: www.eurisol.org
[14] RISP main page: www.risp.re.kr/eng/pMainPage.do
[15] Tshoo K *et al* 2013 *Nucl. Instrum. Methods* B **317** 242
[16] Blumenfeld Y, Nilsson T and Van Duppen P 2013 *Phys. Scr.* **T152** 014023
[17] Kelić A, Ricciardi M V and Schmidt K-H 2009 *Bulg. Nucl. Soc. Trans.* **13** 98
[18] Alvarez-Pol H *et al* 2010 *Phys. Rev.* C **82** 041602
[19] Vonta N *et al* 2016 *Phys. Rev.* C **94** 064611
[20] Flavigny F *et al* 2017 *Phys. Rev. Lett.* **118** 242501
[21] Tarasov O B *et al* 2009 *Phys. Rev.* C **80** 034609
[22] Lukyanov S *et al* 2009 *Phys. Rev.* C **80** 014609
[23] Kurtukian-Nieto T *et al* 2014 *Phys. Rev.* C **89** 024616
[24] Caballero-Folch T *et al* 2016 *Phys. Rev. Lett.* **117** 012501
[25] Samantaria C *et al* 2015 *Phys. Rev. Lett.* **115** 192501
[26] Meisel Z *et al* 2016 *Phys. Rev.* C **93** 035805
[27] Volkov V V 1978 *Phys. Rep.* **44** 93
[28] Dasso C H, Pollarolo G and Winther A 1994 *Phys. Rev. Lett.* **73** 1907
[29] Corradi L, Pollarolo G and Szilner S 2009 *J. Phys. G: Nucl. Part. Phys.* **36** 113101
[30] Corradi L *et al* 2013 *Nucl. Instrum. Methods Phys. Res.* B **317** 743
[31] Souliotis G A *et al* 2002 *Phys. Lett.* B **543** 163
[32] Souliotis G A *et al* 2003 *Phys. Rev. Lett.* **91** 022701
[33] Beliuskina O *et al* 2014 *Eur. Phys. J.* A **50** 161
[34] Watanabe Y X *et al* 2015 *Phys. Rev. Lett.* **115** 172503
[35] Vogt A, Birkenbach B and Reiter P 2015 *Phys. Rev.* C **92** 024619
[36] Mijatovic T *et al* 2016 *Phys. Rev.* C **94** 064616
[37] Welsh T *et al* 2017 *Phys. Lett.* B **771** 119
[38] Zhu L, Zhang F S, Wen P W, Su J and Xie W J 2017 *Phys. Rev.* C **96** 024606
[39] Sekizawa K 2017 *Phys. Rev.* C **96** 014615
[40] Sekizawa K 2017 *Phys. Rev.* C **96** 041601
[41] Karpov A V and Saiko V V 2017 *Phys. Rev.* C **96** 024618
[42] Wang N and Guo L 2016 *Phys. Lett.* B **760** 236
[43] Yao H and Wang N 2017 *Phys. Rev.* C **95** 014607
[44] Souliotis G A *et al* 2003 *Nucl. Instrum. Methods Phys. Res.* B **204** 166
[45] Souliotis G A *et al* 2008 *Nucl. Instum. Methods Phys. Res.* B **266** 4692
[46] Souliotis G A *et al* 2011 *Phys. Rev.* C **84** 064607
[47] Fountas P N, Souliotis G A, Veselsky M and Bonasera A 2014 *Phys. Rev.* C **90** 064613
[48] Souliotis G A 2009 *Progress in Research* Cyclotron Institute, Texas A&M University http://cyclotron.tamu.edu/progress-reports/2008-2009/cyclotron_progress_2009.pdf
[49] Tassan-Got L and Stephan C 1991 *Nucl. Phys.* A **524** 121

[50] Veselsky M and Souliotis G A 2006 *Nucl. Phys.* A **765** 252
[51] Veselsky M and Souliotis G A 2011 *Nucl. Phys.* A **872** 1
[52] Souliotis G A *et al* 2014 *Phys. Rev.* C **90** 064612
[53] Papa M *et al* 2001 *Phys. Rev.* C **64** 024612
[54] Papa M *et al* 2005 *J. Comput. Phys.* **208** 403
[55] Papa M 2013 *Phys. Rev.* C **87** 014001
[56] Giuliani G, Zheng H and Bonasera A 2014 *Prog. Part. Nucl. Phys.* **76** 116
[57] Vonta N, Souliotis G A, Veselsky M and Bonasera A 2015 *Phys. Rev.* C **92** 024616
[58] Aichelin J 1991 *Phys. Rep.* **202** 233
[59] Souliotis G A 2010 *J. Phys.: Conf. Ser.* **205** 012019
[60] Bondorf J *et al* 1995 *Phys. Rep.* **257** 133
[61] Botvina A S and Mishustin I N 2001 *Phys. Rev.* C **63** 061601
[62] Souliotis G A *et al* 2007 *Phys. Rev.* C **75** 011601
[63] Souliotis G A *et al* 2007 *Nucl. Instrum. Methods Phys. Res.* B **261** 1094
[64] Notani M 2000 *PhD Thesis* University of Tokyo
[65] Notani M *et al* 2007 *Phys. Rev.* C **76** 044605
[66] Zhang X H *et al* 2012 *Phys. Rev.* C **85** 024621
[67] Kwan E *et al* 2012 *Phys. Rev.* C **86** 014612
[68] Tshoo K *et al* 2016 *Nucl. Instrum. Methods Phys. Res.* B **376** 188
[69] Mocko M 2006 *PhD Thesis* Michigan State University
[70] Mocko M *et al* 2006 *Phys. Rev.* C **74** 054612
[71] Mocko M *et al* 2008 *Phys. Rev.* C **78** 024612
[72] Summerer K 2012 *Phys. Rev.* C **86** 014601
[73] Suzuki H *et al* 2013 *Nucl. Instrum. Methods Phys. Res.* B **317** 756
[74] Moller P *et al* 1997 *At. Data Nucl. Data Tables* **66** 131
[75] Cappuzzello F, Agodi C, Carbone D and Cavallaro M 2016 *Eur. Phys. J.* A **52** 167
[76] Bazin D and Mittig W 2013 *Nucl. Instrum. Methods Phys. Res.* B **317** 319
[77] Moller P *et al* 1995 *At. Data Nucl. Data Tables* **59** 185